Published in final edited form as:
*Opt Express*. 2006 April 17; 14(8): 3354–3367.

# Adaptive optics scanning laser ophthalmoscope for stabilized retinal imaging

**Daniel X. Hammer**,
Physical Sciences Inc., 20 New England Business Center, Andover MA 01810

**R. Daniel Ferguson**,
Physical Sciences Inc., 20 New England Business Center, Andover MA 01810

**Chad E. Bigelow**,
Physical Sciences Inc., 20 New England Business Center, Andover MA 01810

**Nicusor V. Iftimia**,
Physical Sciences Inc., 20 New England Business Center, Andover MA 01810

**Teoman E. Ustun**, and
Physical Sciences Inc., 20 New England Business Center, Andover MA 01810

**Stephen A. Burns**
School of Optometry, Indiana University, 800 E. Atwater, Bloomington IN 47405

Daniel X. Hammer: hammer@psicorp.com

## Abstract

A retinal imaging instrument that integrates adaptive optics (AO), scanning laser ophthalmoscopy (SLO), and retinal tracking components was built and tested. The system uses a Hartmann-Shack wave-front sensor (HS-WS) and MEMS-based deformable mirror (DM) for AO-correction of high-resolution, confocal SLO images. The system includes a wide-field line-scanning laser ophthalmoscope for easy orientation of the high-magnification SLO raster. The AO system corrected ocular aberrations to <0.1 μm RMS wave-front error. An active retinal tracking with custom processing board sensed and corrected eye motion with a bandwidth exceeding 1 kHz. We demonstrate tracking accuracy down to 6 μm RMS for some subjects (typically performance: 10–15 μm RMS). The system has the potential to become an important tool to clinicians and researchers for vision studies and the early detection and treatment of retinal diseases.

## 1. Introduction

We have previously described the integration of a retinal tracker into various ophthalmic imaging modalities, including scanning laser ophthalmoscopy (SLO) and optical coherence tomography (OCT), and the enhanced diagnostic capabilities obtained in various applications [1–3]. In general, those systems had limited transverse imaging resolution that often masked the true benefit of tracking. For example, for the estimation of nerve fiber layer thickness in normal and glaucomatous eyes, tracking provided little benefit due to the small spatial gradient of that layer [4].

The recent introduction and clinical development of new high resolution retinal imaging systems may provide the most propitious platform for tracking. Adaptive optics (AO) instruments have been used in ophthalmology for nearly ten years to sense and correct ocular aberrations and provide high transverse resolution imaging [5–6]. AO systems couple a wave-front sensor (e.g., Hartmann-Shack, HS-WS) and a wave-front compensator (e.g., deformable mirror, DM) to actively correct distortions caused mainly by the tear film, cornea, and lens. For adaptive optics systems, the high magnification necessary to resolve small structures such as photoreceptors are concomitant with smaller fields of 1–2 deg (300–600 μm). Eye motion for even the best fixators can be up to 0.5 deg and slew targets of interest out of the field of view lowering the duty factor of useable images from a given session. AO systems also suffer from the requirement that reasonable pupil centration be maintained during wave-front sensing. Thus translational head motion and anterior segment tracking are also uniquely important to these systems. Clinical utility for AO instruments probably also necessitates alternate auxiliary wide-field imaging to place the smaller fields at precise locations on the retina. This is analogous to the general requirement that clinical OCT systems, which generate primarily cross-sectional views, also include a secondary imaging system to display a more traditional *en-face* fundus view. In the case of AO systems, there is often uncertainty about the location of the smaller field relative to global landmarks. Retinal tracking, dual imaging, and a well-designed operator interface will aid in the development of advanced clinical functionality and further progress in vision research.

We have built an adaptive optics scanning laser ophthalmoscope that includes an integrated retinal tracker and an auxiliary wide-field imager (henceforth called tracking adaptive optics scanning laser ophthalmoscope, TAOSLO). The system has many features designed to facilitate clinical ease of use as well as improved quality and increased yield of useable information. The significant finding of this work is the characterization of hierarchical elements of the AO stabilization problem. The system has the potential to be used in a wide variety of applications beyond disease diagnosis, from precision stimulus presentation for vision studies to therapeutic laser targeting of malignant retinal structures [7]. This paper describes the design and features of the TAOSLO system and the results of preliminary tests on normal human subjects.

## 2. TAOSLO system description

### 2.1 Overview

A simplified block diagram of the TAOSLO is shown in Fig. 1. The instruments consists of three main sub-systems: a retinal tracker with wide-field line-scanning laser ophthalmoscope (T-LSLO, or TSLO) to stabilize to fixed and repeatable retinal coordinates and correct for the adverse effects of eye motion, a flying-spot scanning laser ophthalmoscope (SLO) that produces high-magnification confocal images, and an adaptive optics (AO) component that senses wave-front distortion and corrects ocular aberrations. Control of hardware and acquisition and processing of images and data from the sub-systems is accomplished from a single software platform. The system therefore presents to the operator and/or clinician a wide-field view of a large portion of the retina, a high magnification view of a particular region of interest, and a view of the ocular aberrations in both the raw form of wave-front slopes and the refined form of wave-front error map and Zernike coefficient plot.

The TSLO sub-system is similar to that reported previously [1]. The SLO creates an image by detection of a flying-spot raster focused on the retina in a confocal arrangement. The adaptive optics component uses a Hartmann-Shack wave-front sensor and deformable mirror to detect and correct ocular aberrations in a closed loop. The system also includes a port that can be used for delivery of near-diffraction-limited stimulus or therapeutic beams to the retina [7]. Those beams require an external independent focus and are collimated into the port behind the deformable mirror.

### 2.2 Retinal tracker

The retinal tracker stabilizes high magnification images by driving two galvanometers placed at appropriate conjugates within the path of the AOSLO in a “master-slave” configuration. The input to the master control loop is $x$-$y$ error signals generated from the low power track beam (~100 μW measured at the cornea, 1060-nm laser diode, LD) dithered on a retinal feature and detected from a confocal reflectometer. The input to the slave control loop is the scaled position signals from the master galvanometers. The slave tracking mirrors are placed at conjugates to the center of rotation of the eye. This allows line-of-sight tracking (i.e., simultaneous tracking of the pupil and retina from rotational eye motion) because the mirrors pivot about the true axis of rotation of the eye.

Integration of retinal tracking into the AOSLO in a master-slave configuration requires several considerations. The setup requires a one-time calibration (gain and offset) between master and slave mirrors. To allow for tracking on a number of potential targets it is desirable to make the fields of view of the tracker and AO systems disparate. Thus we track on targets anywhere within the >40 deg LSLO field while the AOSLO is designed with optics to produce little distortion over a smaller <15 deg field. Also, the galvanometer control electronics are scaled to the appropriate angular range to maximize dynamic range. We generally track on the lamina cribrosa in the optic disc and image near the fovea – features separated by ~15 deg. This separation results in geometric and torsional eye motion errors because the eye rotates about equatorial axes and cyclo-rotates about an axis centered near the posterior pole. The one-time calibration between master and slave eliminates geometric but not cyclo-rotational errors. The TSLO produces a wider field of view at the expense of increased aberrations that are small relative to the pixel size. Aberrations must be carefully minimized in the AOSLO path due to the high resolution and small pixel size. Therefore, the AOSLO raster cannot pass through the wide-field LSLO imaging optics and must be combined at the pupil in a different manner.

Our integration scheme also allows for nested pupil tracking by adjusting the offsets of the slave and AOSLO raster scanners in a coordinated manner. Because these mirrors are at different conjugates, walking these mirrors within limits with commands derived from both retinal and pupil coordinates (the latter from the HS-WS) can correct for translational head motion. However, to date we have not yet closed the pupil tracking loop. Instead, we examine the combined residual error over AO image sequences with retinal tracking alone in order to estimate the magnitude of pupil translation effects. Advanced tracking schemes including adaptive filtering and tracking scaled to the AOSLO image feature size may be implemented for improved tracking precision. These will be discussed in more detail in Section 5.

### 2.3 Optical setup

The optical setup for the TAOSLO is shown in Fig. 2. We developed a simplified optical arrangement with elements placed on both sides of a vertical plate. This enables access to all components with a smaller system footprint. Spherical mirrors are primarily used to limit back-reflections, minimize chromatic distortion, and reduce dispersive pulse broadening (when using therapeutic ultrafast laser pulses, for example). In our configuration, astigmatism that results from use of spherical mirrors is diminished by operation at near-normal angles of incidence with longer focal lengths to accommodate the desired AOSLO field angles (±6 deg). Pair-wise orthogonal mirror relays automatically cancel most of the astigmatism.

The front-end TSLO uses a 909-nm superluminescent diode (SLD, ~200 μW, 20-nm bandwidth) for wide-field imaging. A line fanned out by a cylindrical lens (CL) is scanned on the retina and de-scanned back to a linear array detector (LAD) with a single galvanometer in a confocal manner [8]. Custom objectives (O3 and O4) transfer retinal image back to the detector and an ophthalmoscopic lens (OL) relays and focuses the image onto the retina. The tracker uses 8-kHz resonant scanners (RS) to dither on a circle and a confocal reflectometer and phase-sensitive detection scheme to driver the master tracker galvanometers (TG) according to the motion of the eye. An InGaAs avalanche photodiode (APD) is used for tracker beam detection. An 8×8 LED array is used for fixation.

Although it is possible to use the SLO imaging beam to also sense ocular aberrations with the wave-front sensor, higher throughput and off-axis operation (to minimize corneal reflections) are achieved with two separate beams. The imaging beam (800±15-nm SLD, ~300 μW) and the wave-front sensing beam (also called the AO beacon, 670-nm LD, ~35 μW) are thus at different wavelengths. LSLO imaging, tracking, SLO, AO beacon and fixation wavelengths are combined with custom dichroic beamsplitters (D1-5). The power levels for completely overlapping beams are greater than a factor of 2 below the ANSI laser safety limits.

The AOSLO beams are directed from the vertical plate through a front pair of objectives (O1 affixed to the plate and O2). Both off-the-shelf and custom lenses have been used in the relay successfully. The custom lenses were designed to minimize spherical and chromatic aberrations and control field flatness. Focus for the high-magnification image is independent of TSLO focus and is accomplished by adjustment of the DM stage (fine) and the stage on which the plate rests (coarse), the latter controlling separation between O1 and O2. Coarse focus adjustments of up to 10 diopters are achieved. DM stage (fine) focus controls the separation between beacon focal plane and the AO raster focal plane allowing systematic shifts of focus, such as those due to longitudinal chromatic aberration, to be compensated.

A standard approach is used for the SLO optical setup, whereby a flying spot is scanned on the retina and de-scanned through the same optics back to a confocal pinhole, often with unequally-sized entrance and exit pupils [9]. Our system is designed for a 6-mm pupil (entrance and exit) and uses either a 100 or 200-μm pinhole (15 or 30-μm referenced to the retina). The SLO raster is created with a 12-kHz resonant scanner in the fast horizontal axis (RSh) and a galvanometer in the slower vertical axis (Gv), both placed at pupil conjugates to pivot the retinal raster from the pupil. Because voltage offsets cannot be applied to a resonant scanner, we have placed this scanner on an additional large, slow galvanometer (OG). This, together with a voltage offset applied to Gv, allow the raster to be rapidly positioned under computer control anywhere within the field of view. This can be used for the acquisition of automatic montages described in Section 4. The slave galvanometers (SGh and v) are placed at conjugates to the center of rotation for line-of-sight tracking. Spherical mirrors (SM5-8) relay the SLO imaging beam and the AO beacon through the scan engine to the eye and back again. A pellicle beamsplitter (92%T/8%R) is used to couple the beacon into the instrument.

On the rear side of the plate, SM1-4 direct the SLO source (and stimulus or therapeutic laser source, if used) off the deformable mirror to the eye and return backscattered light from the retina to the wave-front sensor and SLO detector (APD) via confocal pinhole (100 and 200-μm diameter). The Hartmann-Shack wave-front sensor (HS-WS) is comprised of a 65×65-element lenslet array (0.4-mm pitch and 25-mm focal length) and a 1024×1024-pixel, 12-mm CCD camera (Dalsa Inc.) with a maximum frame rate of 60 Hz. A 141-element, 4.8-mm, MEMS-based, continuous-surface, electrostatic-actuator-driven DM (Boston Micromachines Inc.), with maximum stroke of ~4 μm, is used for wave-front correction. The spherical mirrors are chosen to de-magnify a 6-mm pupil to 3.8-mm at the resonant scanner and deformable mirror and magnify it to 7.7-mm at the wave-front sensor.

### 2.4 Electronics and instrumentation

Tracking functions are performed by a set of stacked electronics boards. The control and processing electronics use a field programmable gated array (FPGA) chip to perform digital lock-in amplification and other pre-processing steps and a digital signal processor (DSP) to execute two real-time proportional-integral-derivative (PID) control loops (for master and slave systems). The DSP has a loop rate of 62.5 kHz for a closed loop bandwidth in excess of 1 kHz (up to the mechanical limit imposed by the scanner response). Analog-to-digital and digital-to-analog converters (ADC and DACs) receive reflectometer and galvanometer position signals and output galvanometers drive signals. Communication between the tracking boards and host computer is accomplished via a USB interface. The main system software sends control and calibration parameters to the tracking board, which in turn passes reflectance, position, and error signals back to host processor. The control loop includes an automated blink detection and track re-lock algorithm that has been described previously [2].

Besides the tracking boards, system electronics include three framegrabbers (analog for SLO, digital for LSLO and WS), galvanometer driver boards, custom LSLO camera board, LED fixation driver board, and custom system timing board. Since the master and slave control loops are closed via software, the electronic control loop resident on the driver boards is by-passed for the tracking galvanometers. All other imaging and offset galvanometers use the electronic control loop. The small electronic board that drives the LED array for fixation is controlled by simple commands over the serial port. The custom timing board provides horizontal (line) and vertical (frame) sync signals and a non-linear pixel clock to the analog framegrabber to automatically linearize the sinusoidal scan produced by the resonant scanner Small phase errors in the generated non-linear pixel clock and the actual scanner output can cause distortion on one side of the frame where the sinusoidal scan is flat and the pixel clock sampling is sparse (i.e., approximately the first 50 pixels). The sync signals also drive the WS external synchronization signals and the SLO SLD source for modulation, which creates a blanking region for the analog framegrabber. Tracking in this configuration prohibits a fixed physical mask to be used for blanking. The LSLO and SLO systems are not synchronized since they use entirely independent optical paths. The LSLO camera acquires a 512×512-pixel frame at 15 frames/sec. The 12-kHz SLO resonant scanner frequency enables a 512×512-pixel frame rate up to ~25 frames/sec. In practice, we operate at half that speed since the images from all three components (LSLO, SLO, and WS) are acquired and displayed by a single software platform.

## 2.5 AO control software and user interface

The system software performs two primary tasks: adaptive optics control and acquisition, display, and processing of the LSLO, SLO, and WS images. All operations were performed on a single 3.1 GHz-processor computer. The retinal tracking control loop runs in real-time independently of the host, so processor resources are freed for essential AO and imaging operations. The adaptive optics operations include WS spot position and slope calculation, AO (WS/DM) calibration, AO closed-loop operation, and wave aberration and Zernike coefficient calculation. Secondary software tasks include communication with the tracking board, display and logging of tracking signals, streaming to disk of videos (from all three cameras), and single image acquisition in a variety of formats. When a live video is streamed to disk, two additional files are saved that contained track data (reflectance, *x-y* track mirror positions, and either the *x-y* error signals or the *x-y* slave mirror positions) in binary format and a text file that contained all system parameters and calibration factors.

For AO-correction using the continuous-surface DM, a one-time calibration is performed subsequent to system alignment to find the influence of each actuator on its neighbors and to establish a baseline for calculation of slopes. The software uses a standard algorithm for spot centroid determination that operates at the frame rate of the WS camera up to 30 Hz. During AO-correction, the local wave-front slopes are found and inverted with a pseudo-inverse function and fed to the DM driver. The wave aberration function and Zernike coefficients can be calculated in real-time, though this is not usually done during measurement to preserve processor resources for more critical functions. The closed-loop bandwidth of the AO system is ~2–3 Hz. Streaming videos requires processing and often slightly reduces the frame rate further (to the 8-Hz frame rate presented in this paper). The reduction in frame rate, however, did not lower the overall rate for the wave-front sensing and AO correction from 12 Hz.

## 3. Preliminary human subject test plan

The TAOSLO system was tested in a limited number of human volunteers with healthy eyes aged 26 to 49 (5 men, 1 woman, mean age = 36) to characterize AO-corrected imaging performance and retinal tracking accuracy. Because of the protocol, human subjects were tested non-mydriatically (i.e., with 3–5-mm natural pupils), so we expected less than optimal imaging performance than had a 6–7 mm pupil been used. Since the correction was across a smaller pupil than the system was designed for, the DM was always under-filled and mirror edge effects did not confound the measurement. The subjects used a chin rest but not a bite-bar. Figure 3 shows a photograph of the system during testing.

Prior to examination, informed consent was obtained from all subjects. A typical session included acquisition of several video sequences ≥10 seconds in duration for comparison of imaging modes in a number of conditions. Tracking and AO were tested in all subjects by simple qualitative comparison of the videos with and without tracking or adaptive compensation. Advanced scan routines such as automated montages were acquired on several of the volunteers. A montage in this sense is a 1.5×1.5-mm (5×5-deg) image with <1-μm pixels pieced together automatically from an array of single SLO frames. Auxiliary data collected included wide-field LSLO images, wave-front slopes (from which the Zernike coefficients, wave-front error map and point spread function were calculated), and track position data.

## 4. Results

Qualitative improvement in AO imaging was found in all subjects. We were able to resolve the cone mosaic in all subjects, although it was sharper in younger subjects who generally had better ocular optics and less aberrations in the smaller (undilated) pupil. We were able to track on all subjects and when it was used, the blink/re-lock algorithm worked well to re-position and re-lock the tracker after blinks on the same target as before the blink.

### 4.1 AO performance

To characterize the performance of the AO system to dynamically correct aberrations, we acquired and processed two ~10 sec. videos from the SLO and WS cameras in which AO correction was active for half of the video frames. For the WS video, the Zernike coefficients and wave-front error map were calculated in a typical manner [10]. Figure 4 shows the results.

The subject in this case had a 4.5-mm pupil and the SLO images were acquired at an eccentricity of 3 deg. The cone mosaic is clearly visible in Fig. 4(a) and cones measure ~5–6 μm in diameter in agreement with previous measurements at this eccentricity [11]. Figures 4(b) and 4(d) represent the wave-front error map (full scale = ± 2 μm) averaged over those video frames acquired with and without AO correction, respectively. The mean (min-max) RMS error was 0.08 (0.02–0.13) μm with AO correction and 0.78 (0.55–1.16) without AO correction. Figure 4(e) is the RMS error separated by Zernike order and also averaged over corresponding frames acquired with and without correction. This plot indicates that both lower and higher order aberrations are corrected by the system.

We also compared the contrast of the images in Figs. 4(a) and 4(c) to obtain another quantitative measure of AO improvement. When measured in a region of interest (ROI) that measured 50×50 pixels in the center of the image, the Michelson contrast increased from 0.20 to 0.50. Another measure of contrast improvement is the standard deviation of the image histogram, which increased from 37.9 to 52.4 when measured across the entire and nearly doubled when measured in an ROI that included only cones from 23.9 to 40.3.

Figure 4(f) plots the AO correction as a function of time for the data shown in Figs. 4(b), 4(d), and 4(e) and also for a second subject with lower uncorrected ocular aberrations (with a 5-mm pupil). The mean (min-max) RMS error for subject 2 was 0.09 (0.04–0.14) μm with AO correction and 0.29 (0.24–0.35) without AO correction. For subject 1, the video was acquired with the AO on and then off and vice versa for subject 2 so only the data on subject 2 yielded a meaningful rise-time and hence AO closed-loop bandwidth. The 10%−90% rise-time measured for subject 2 was 0.36 sec for a measured closed-loop bandwidth of 2.8 Hz.

### 4.2 Retinal tracking performance

Accurate calibration between master and slave tracking systems is an essential factor that determines tracking accuracy. Figure 5 shows the master and slave positions recorded from galvanometer shaft optical sensor for a relatively long scan (~18 sec.). Since the master tracker is set to operate over a larger angular range than the slave, the eye motions shown here take up a smaller amount of the dynamic range reserved for the master tracker. The master tracker signals therefore have more quantization noise. Except for the saccades of >0.25 deg, the slave followed the master positions nearly exactly. However, empirical PID slave gain optimization (de-tuning) was used to find a reduced gain which limited the transfer of high bandwidth tracking noise from the master signals. This is the reason that the slaves follow well with reduced noise except during the faster saccades (where frames may be corrupted anyway). For the entire data set shown in Fig. 5, the mean ± standard deviation difference between master and slave was 4.4±3.9 μm for the $x$-axis and 6.7±8.3 μm for the $y$-axis.

Figures 6–9 illustrate AO imaging with retinal tracking on a young, healthy subject with good fixation. The subject was able to maintain fixation to within ~0.5–1 deg of the target. The videos were acquired at an eccentricity of ~2 deg and the cones measured ~5–6 μm in diameter. There is some distortion on the left side of the video frames that resulted from improper alignment of the pupil. When tracking was engaged, the tracking mirror positions were recorded. In Figs. 6 and 7, we followed a single cone for the duration of the video clip and the cone position is shown in plots to the right of the video. For the non-tracking case shown in Fig. 6, toward the end of the video sequence when the original cone moved completely out of the frame, we jumped to alternate cones and the displayed positions are corrected to account for those jumps. Figure 6 shows primarily horizontal motion.

Figure 7 shows the case with the tracker engaged. The plot in Fig. 7(a) shows the mirror position, which signifies the uncorrected eye position, on the same scale as the cone position, which signifies the stabilized eye positions. The cone positions are shown on a smaller scale in Fig. 7(b). The RMS deviation from mean for the non-tracking case is 84 and 31 μm in the $x$- and $y$-axis, while for the tracking case is 6 μm for both axes. Figure 7 also illustrates the relock algorithm as two blinks occurred at ~1.5 and 5 sec.

Figure 8 shows the case for simple post-processing, software-assisted registration. In this case, the cone positions recorded for Fig. 7 were used to shift the frame. We have also developed relatively simple software that is able to determine the appropriate shifts from two-dimensional cross-correlation of a region-of-interest within the frame.

Figure 9 summarizes the stabilization accuracy with tracking and software registration. Shown are composite images generated by co-adding all the frames from the videos shown in Figs. 6–8 excluding those frames with blinks. (The blink frames didn't alter the appearance of the composite images appreciably and accounted for only 5–10% of frames.) The degree to which tracking corrects eye motion can be seen by comparison of Figs. 9a and b. The vessel is completely washed out in Fig. 9(a) but the boundary remains clear in Fig. 9(b). The cone mosaic is not resolved in Fig. 9(b), although the mottled appearance suggests only a small amount of residual position error. That residual position error is eliminated with software registration as indicated by the composite image in Fig. 9(c). Note that in this case the registration accuracy exceeds a single cone as evidenced by the fact that the cone mosaic is still resolved. Line profiles through three cones are shown in Fig. 9(d) for the composite image, Fig. 9(c), in comparison to a single frame (not shown). The line profiles for the composite image are smoother while there is only a small degradation in contrast. For 10 cones measured across the images, the ratio of contrast between the composite and single frames ranged between 0.45 and 0.85.

### 4.3 Automated montage

To illustrate the potential for advanced imaging techniques with the TAOSLO, we present the automated acquisition of montages from 2 subjects. A 4×4 array of 1-deg SLO images was acquired with ~20% overlap for a total field size of ~3.5-deg (~1 mm) at an eccentricity range of ~2–6 deg. The cones in these frames have a measured diameter in the range of 5–7 μm. Figure 10 is an LSLO video from the first subject showing the macular montage acquisition in the large field. The video overlay displays exactly what the acquisition software displays to the user.

Figure 11 shows an SLO video of a similar sequence from a second subject (with better ocular optics). The video begins without AO-correction and the sequence is initiated soon after the AO is turned on (watch the indicators at the bottom of the frame). Five frames are acquired at each position in the 4×4 array. In this video, there is a quick blink/loss-of-lock/relock at ~11 sec.

Figure 12 shows the montage created from the video in Fig. 11. Because of the automated manner in which the images were acquired, the montage took very little time to assemble. The frames during loss-of-lock (positions from lower left corner: 3,0 and 0,1) were unusable because the tracker was being reset, although this again illustrates the degree to which the tracker assisted by the re-lock algorithm is able to return to fixed retinal coordinates. Other advanced techniques such as scan suspension during re-lock have been used in other tracking systems [2] and will be implemented in the future. The cone mosaic can be seen throughout the montage though some warping is seen at a few positions. The overall precision of the tracking system can be characterized by viewing the edge of the montage, where errors cause one image to shift with respect to another.

## 5. Discussion

Motion-induced blur will always plague imaging in general and imaging the eye in particular. As new high resolution instruments are developed, the problem of motion is correspondingly magnified. We have developed a retinal imaging instrument that actively compensates for eye motion to within an RMS error of 6 μm for some and 10–15 μm for most subjects, regardless of their ability to fixate. We have also described other features of the system designed to improve clinical usefulness.

The AO system corrected ocular aberrations in all subjects to less than ~0.1 μm RMS wave-front error with a closed loop bandwidth of a few Hz. This bandwidth, although not high, is sufficient to compensate for the majority of dynamic aberrations resulting mostly from changes in the tear film layer. Because none of the subjects was dilated, transverse resolution and depth of focus was not optimal.

The source of the residual distortion in the AOSLO single and composite images in Figs. 4–10 was due either to systematic instrumentation and tracker errors or uncorrected motion and alignment artifacts. The former includes expansion of the first ~50 pixels of all individual frames caused by phase errors in the generated non-linear pixel clock. It also includes errors inherent to the system itself: the tracker can only work when finite errors exist. The magnitude of these errors depends upon the target selected and how well the dither beam size and amplitude match that target as well as the tracking stability at a given control loop gain and SNR. The finite error signal SNR at full tracking bandwidth results in position jitter noise. As discussed above, geometrical errors occur and scale with the distance between the tracking and image beam but can be eliminated with proper master-slave calibration. Slave tracking fidelity depends upon the accuracy (and degree of linearity) between master and slave trackers. Also, speckle-like perturbations may arise from the heterogeneous reflectance profile of the retina. Finally, given the long depth of focus of the tracking confocal reflectometer, scattered or reflected light from the anterior segment may contribute to the tracking errors. The tracking errors are generally isotropic and cause distortion in a single image and a small translation of frames in the composite image.

Uncompensated high frequency motion will affect individual frames and depending upon frequency and direction with respect to the line and frame rate, may exhibit image compression, expansion, or shear. Low frequency uncompensated motion will affect composite images generated from multiple frames and can lead to translation, magnification, and rotation of one frame with respect to another. Since the contrast in the composite image generated after software registration (which corrects all translation between frames) showed little variation across the frame, higher frequency motion, magnification, and rotation do not contribute much to the residual distortion. Cyclo-rotation remains uncorrected in the current configuration but since there is little difference in peripheral blurring between single and composite images, this error is also thought to be small. The error thought to contribute the most to the distortion in individual frames is pupil shifts and misalignment that cause beacon or AOSLO beam vignetting, and thus improper AO correction across the entire pupil. This problem will be less evident in dilated patients and can be actively controlled when pupil tracking is implemented.

Despite the benefits of retinal tracking presented here, we wish to improve the overall accuracy of the tracking system and reduce the error to less than 5 μm (<1 cone diameter for cones at 2 deg eccentricity). A number of strategies to address these issues are being investigated in on-going research and development to improve real-time tracking precision and imaging data yield. For example, by simply applying a threshold to the tracking velocity, video frames can be rejected (and not saved) when transient tracking errors are known to be most severe. We may improve tracking fidelity by selection of smaller features with a corresponding reduction in dither beam size and amplitude. Moreover, geometric errors are reduced by using tracking features closer to the image AOSLO field. Due to the inherent safety margin of its scanned line, the LSLO imaging speed is scalable to hundreds of Hz and could eventually be used for real-time and post-processing corrections of errors, including those attributed to cyclo-rotation. Position signal error noise and jitter, as well as slave fidelity can be addressed concurrently with appropriate adaptive filtering algorithms. These algorithms must eventually be coordinated with pupil position data to enable high order optical distortion to be compensated. Moreover, the algorithms are being designed with the recognition that full tracking bandwidth is only required for brief periods during rapid saccades. For a majority of the quiescent time between saccades, the eye drifts only slowly. Therefore by reduction of the slave tracking bandwidth, the SNR and tracking fidelity can be improved. This trade-off carries the price of more frequent loss-of-lock but may yield a greater fraction of distortion-free images per session. Reduction of reflectance perturbations may occur with the use of broadband sources for the tracking beam. Also, distortions related to imprecise pupil centration will be substantially eliminated with full pupil tracking. Finally, all of the available tracking signals can be used deterministically in post-processing de-warping software for even finer registration [12].

These advances will aid in the development of new applications for adaptive optics in ophthalmology. One potential area is in the selective targeting of retinal pigment epithelial cells for the treatment of age-related macular degeneration [13]. We have begun to investigate adaptive optics in combination with other technologies for that application [7]. Future studies will explore many avenues of inquiry related to understanding the fundamental mechanisms of vision and the diagnosis and treatment of diseases which affect vision.

## Acknowledgments

This work was supported by NIH grants R21EB003111 and R01EY14375.

## References and links

1. Hammer DX, Ferguson RD, Magill JC, White MA, Elsner AE, Webb RH. Image stabilization for scanning laser ophthalmoscopy. Opt Express 2002;10:1542–1549. [PubMed: 19461690]
2. Hammer DX, Ferguson RD, Iftimia NV, Ustun TE, Wollstein G, Ishikawa H, Gabriele ML, Dilworth WD, Kagemann L, Schuman JS. Advanced scanning methods with tracking optical coherence tomography. Opt Express 2005;13:7937–7947. [PubMed: 19498823]
3. Ferguson RD, Hammer DX, Elsner AE, Webb RH, Burns SA, Weiter JJ. Wide-field retinal hemodynamic imaging with the tracking scanning laser ophthalmoscope. Opt Express 2004;12:5198–5208. [PubMed: 19484077]
4. Ishikawa, Hiroshi; Gabriele, Michelle L.; Wollstein, Gadi; Ferguson, R Daniel; Hammer, Daniel X.; Paunescu, L Adelina; Beaton, Siobahn A.; Schuman, Joel S. Retinal Nerve Fiber Layer Assessment Using Optical Coherence Tomography (OCT) with Active Optic Nerve Head Tracking. Inv Ophthalmol Vis Sci 2006;47:964–967.
5. Liang J, Williams D, Miller D. Supernormal vision and high-resolution retinal imaging through adaptive optics. J Opt Soc Am A 1997;14:2884–2892.
6. Roorda A, Romero-Borja F, Donnelly W III, Queener H, Hebert T, Campbell M. Adaptive optics scanning laser ophthalmoscopy. Opt Express 2002;10:405–412. [PubMed: 19436374]
7. Hammer, DX.; Ferguson, RD.; Bigelow, CE.; Iftimia, NV.; Ustun, TE.; Noojin, GD.; Stolarski, DJ.; Hodnett, HM.; Imholte, ML.; Kumru, SS.; McCall, MN.; Toth, CA.; Rockwell, BA. “Precision targeting with a tracking adaptive optics scanning laser ophthalmoscope” paper 6138–37. In: Manns; Soderberg; Ho, editors. Ophthalmic Technolgies XVI. 2006.
8. Hammer DX, Ferguson RD, Ustun TE, Bigelow CE, Iftimia NV, Webb RH. Line-scanning laser ophthalmoscope. J Biomed Opt. (Special Issue for A. J. Welch) in press.
9. Webb RH, Hughes GW, Delori FC. Confocal scanning laser ophthalmoscope. Appl Opt 1987;26:1492–1497. [PubMed: 20454349]
10. Thibos LN, Applegate RA, Schwiegerling JT, Webb R. Standards for reporting the optical aberrations of eyes. J Refractive Surg 2002;18:S652–S660.
11. Curcio CA, Sloan KR. Packing geometry of human cone photoreceptors – variation with eccentricity and evidence for local anisotropy. Visual Neuroscience 1992;9:169–180. [PubMed: 1504026]
12. Vogel C, Arathorn D, Roorda A, Parker A. Retinal motion estimation in adaptive optics scanning laser ophthalmoscopy. Opt Express 2006;14:487–497. [PubMed: 19503363]

13. Alt C, Framme C, Schnell S, Lee H, Brinkman R, Lin CP. Selective targeting of retinal pigment epithelium using an acousto-optic laser scanner. J Biomed Optics 2005;10:064014.

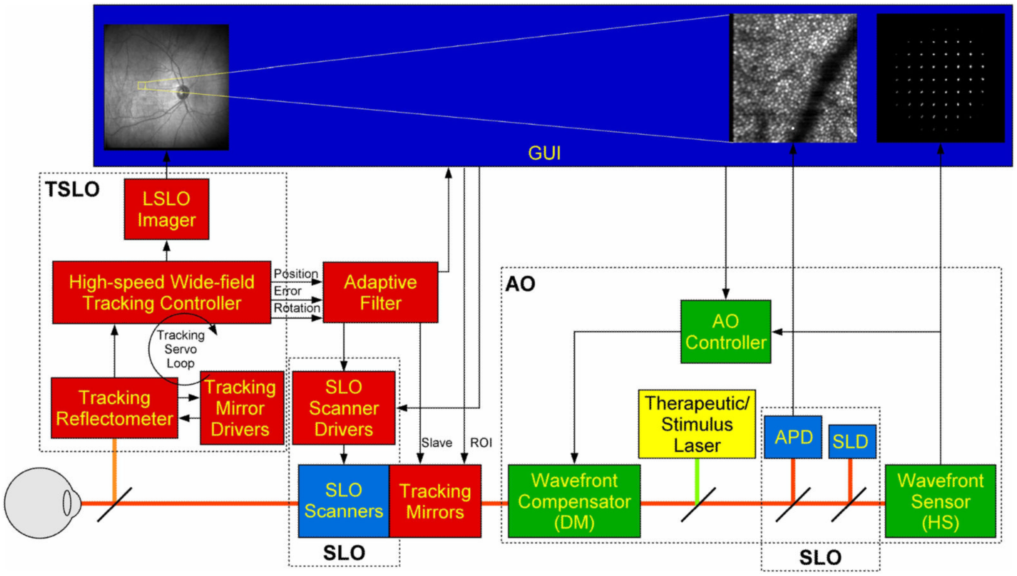

**Fig. 1.**

TAOSLO block diagram. Tracker components are shown in red, SLO components are shown in light blue, AO components are shown in green, and the external therapeutic/ stimulus port is shown in yellow.

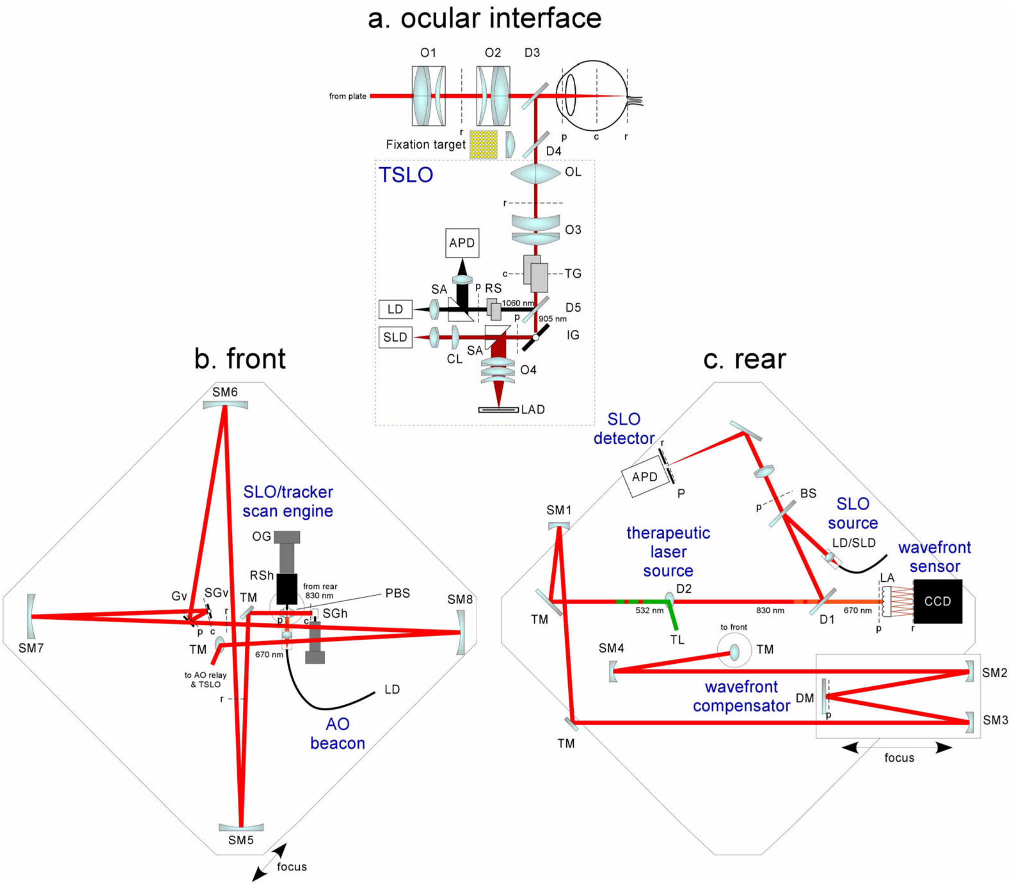

**Fig. 2.**

TAOSLO optical layout. (a) Ocular interface which includes TSLO and front lens relay, (b,c) View of front and rear of vertical plate on which optics are mounted. Entire plate is mounted on a stage to control focus between front lens relay. Positions of conjugates to retina, pupil, and the center-of-rotation of the eye are indicated (with lower case p, c, r). Dx: dichroic beamsplitters, Ox: custom objectives, OL: ophthalmoscopic lens, TG: master tracking galvanometers, RS: resonant scanners, SA: split aperture, CL: cylindrical lens, LD: laser diode, SLD: superluminescent diode, APD: avalanche photodiode, LAD: linear array detector, TM: turning mirrors, SMx: spherical mirrors, SGh and SGv: slave galvanometers, Gv: SLO raster galvanometer, RSh: SLO raster scanner, OG: offset galvanometer, PBS: pellicle beamsplitter (92/8), DM: deformable mirror (on stage for additional focus adjust), TL: therapeutic laser port (with independent focus), BS: beamsplitter (50/50), LA: lenslet array.

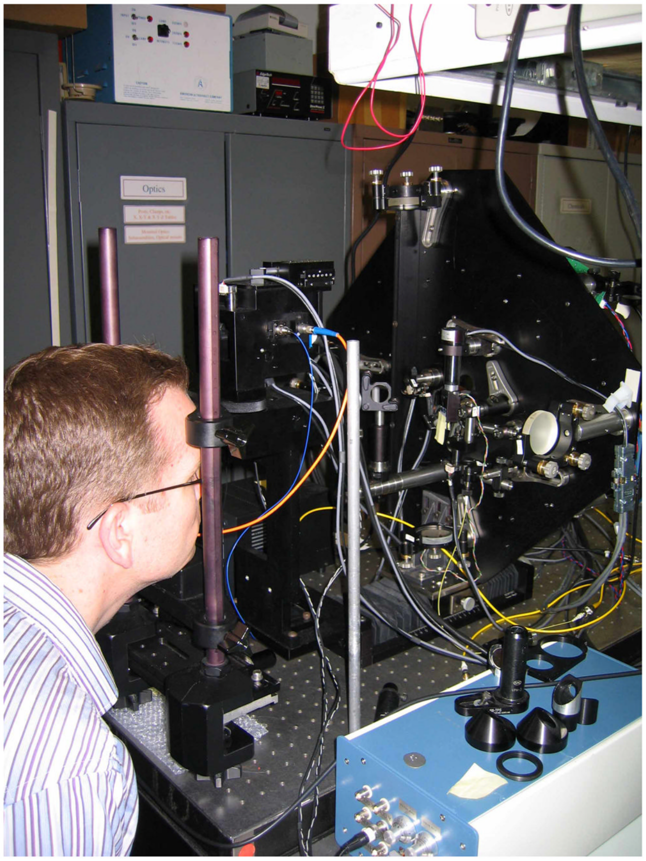

**Fig. 3.**

Photograph of TAOSLO during human subject testing.

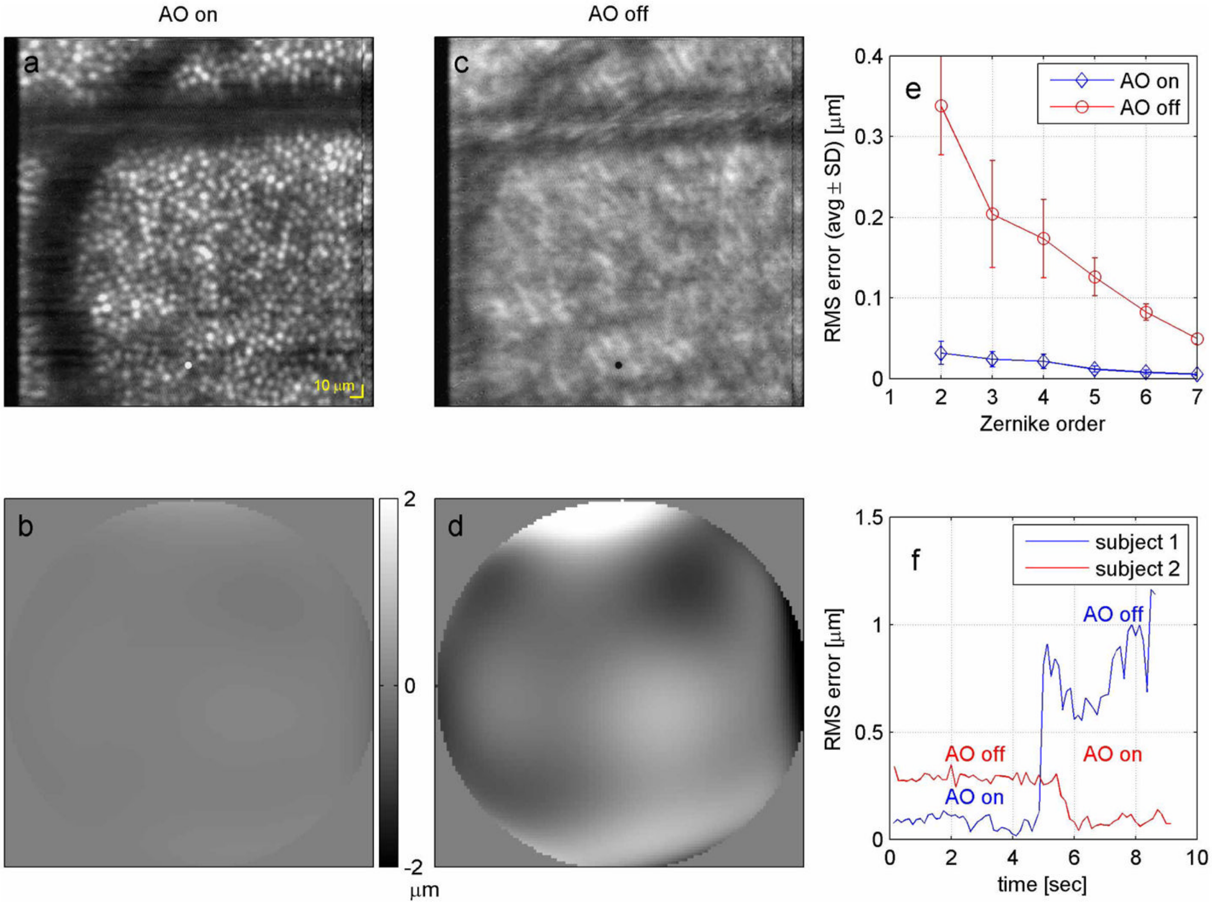

**Fig. 4.**

Summary of AO performance. (a) SLO image acquired with AO correction. (b) Wavefront error map averaged over all video frames during AO correction (~5 sec.) for 4.5 μm pupil. (c) SLO image acquired without AO correction. (d) Wave-front error map averaged over all video frames when AO was off (~4 sec.). (e) RMS wave-front error by Zernike order averaged for all video frames with and without AO correction. (f) Temporal dynamics of RMS wave-front error.

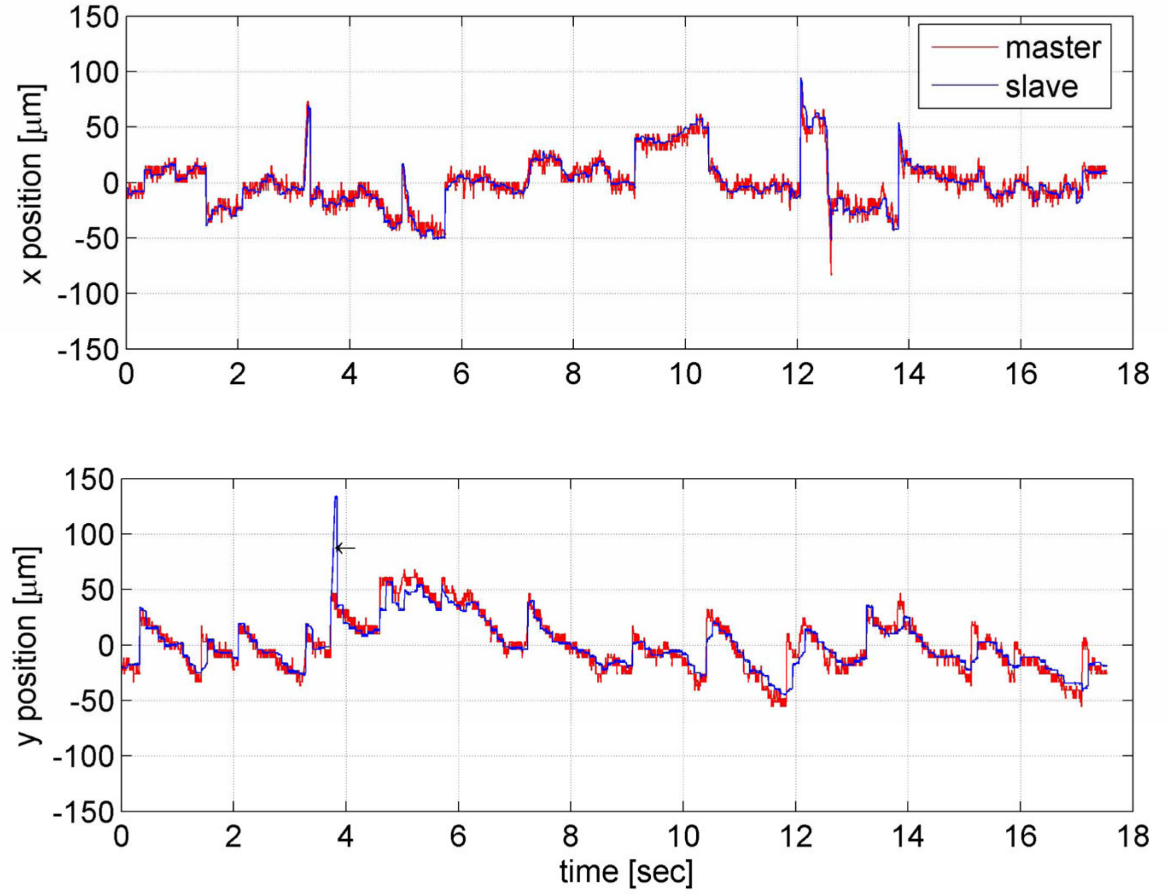

**Fig. 5.**
Master and slave mirror positions show good correspondence during a relatively long scan (~18 seconds). One saccade indicated by the arrow caused a large overshoot in the slave *y* position due to the limiting of the slave PIS bandwidth.

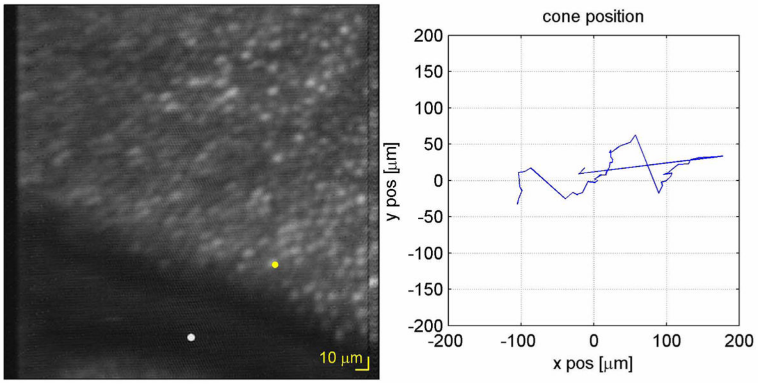

**Fig. 6.**

(1.6 Mb) Video of retina with adaptive correction without tracking for a young, healthy subject with good fixation (7 sec.). The plot shows the position of the cone indicated by the yellow circle in the video.

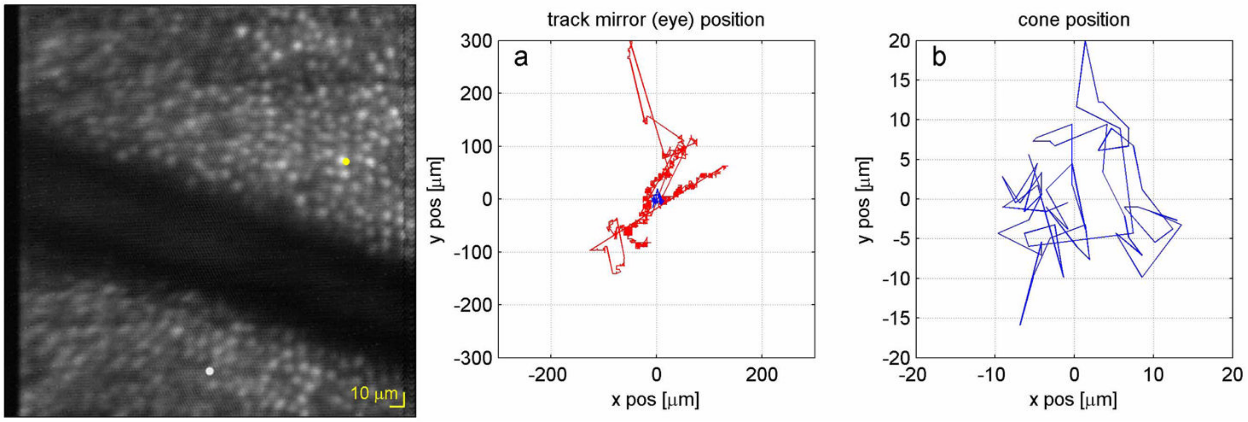

**Fig. 7.**

(2.9 Mb) Video of retina with adaptive correction with tracking for the same subject as Fig. 6 (9 sec.). (a) The tracking mirror position, which represents the (uncorrected) eye position, is shown in red along with the cone position, which represents the corrected eye position, in blue and indicated in the video by the yellow circle. (b) The cone position is shown on a magnified scale.

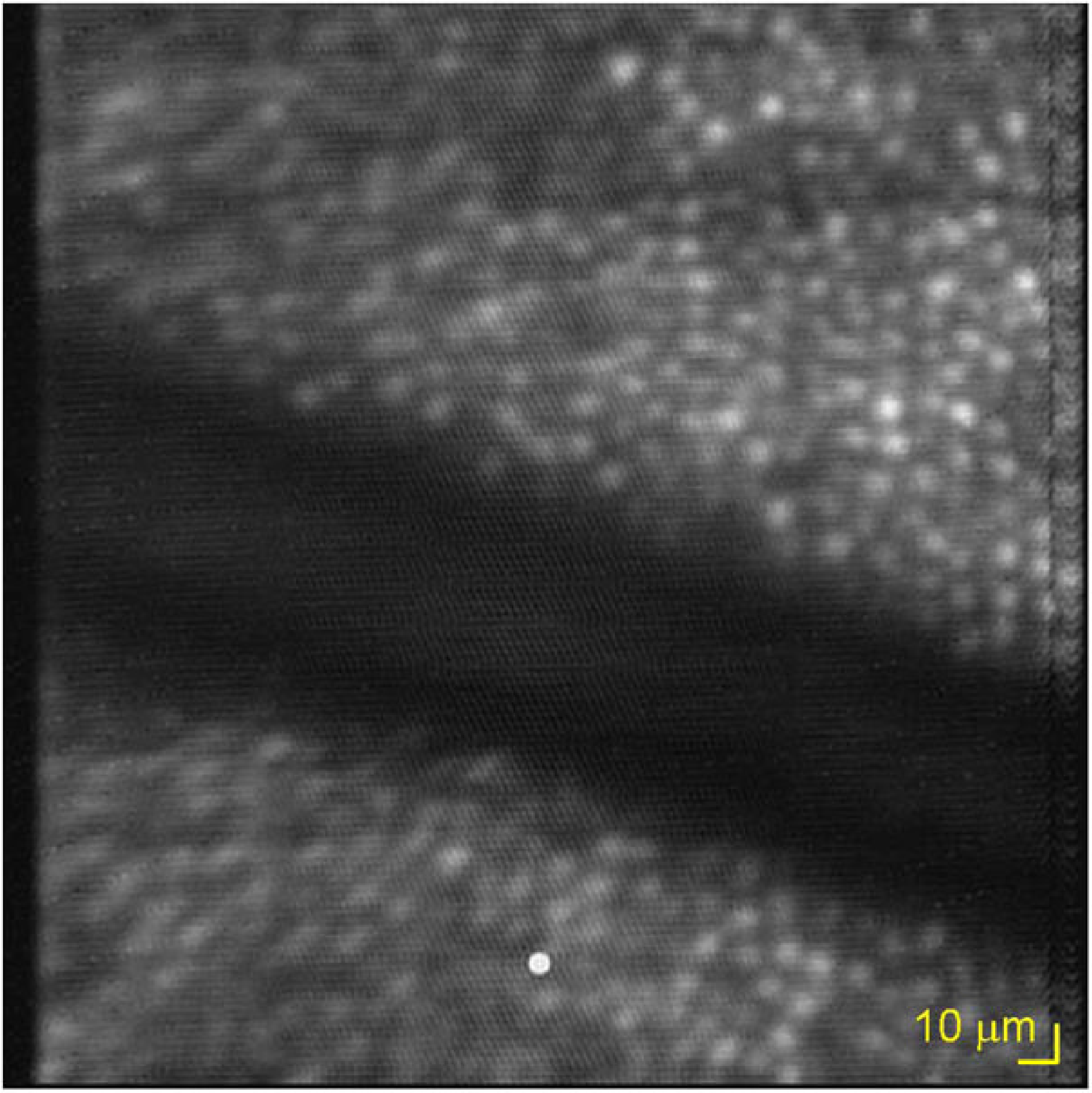

**Fig. 8.**
(1.4 Mb) Video of simple software-assisted registration for the video shown in Fig. 7.

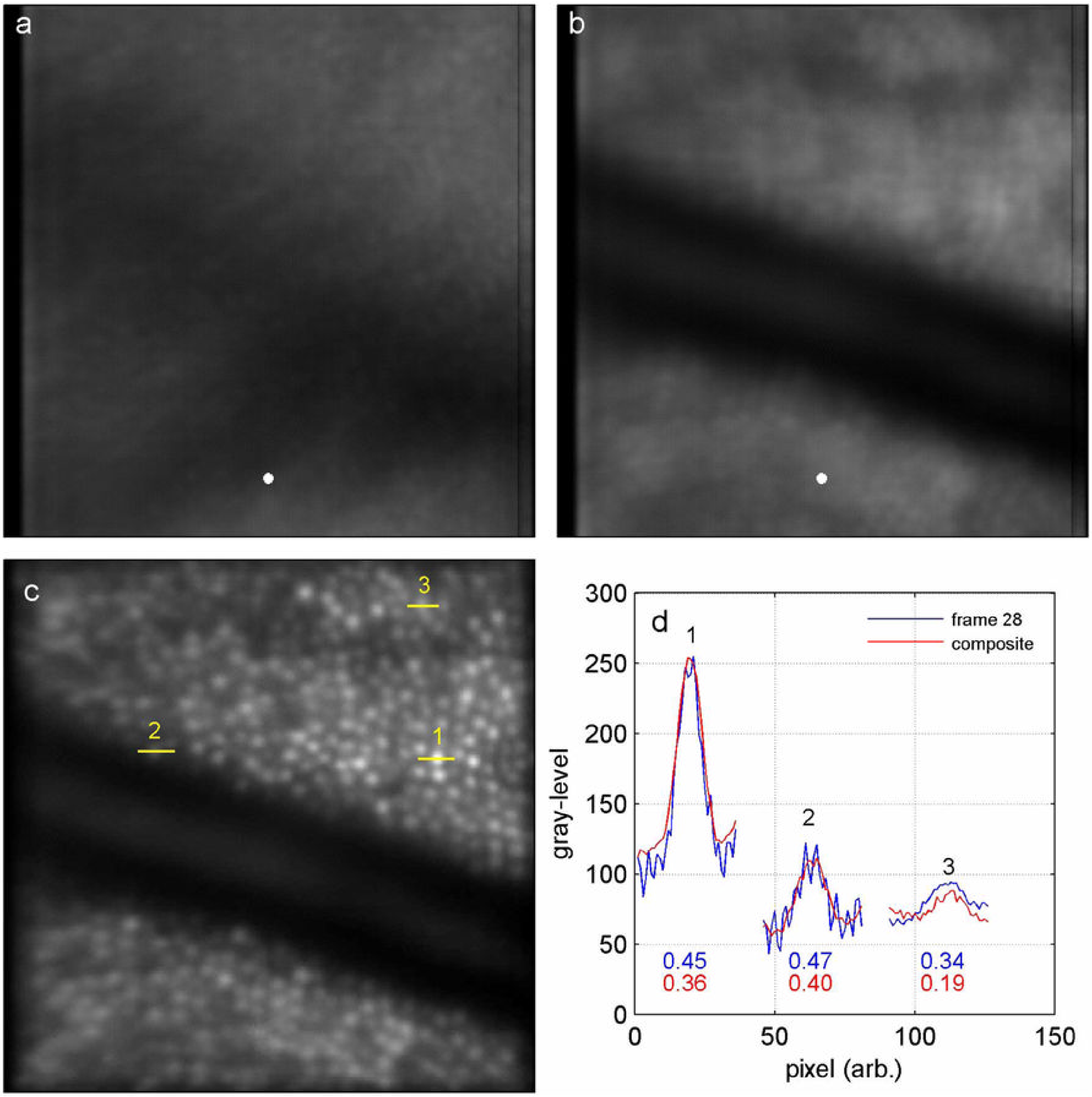

**Fig. 9.**

Summary of tracking and registration results. Composite images generated from co-added frames (blinks excluded) for (a) non-tracking (52 frames), (b) tracking (67 frames), and (c) software registration (67 frames) cases from the videos displayed in Figs. 6–8. Line profiles (d) through three cones labeled in (c) in a single unprocessed frame (28) and the composite image. Contrast values are shown below the curves.

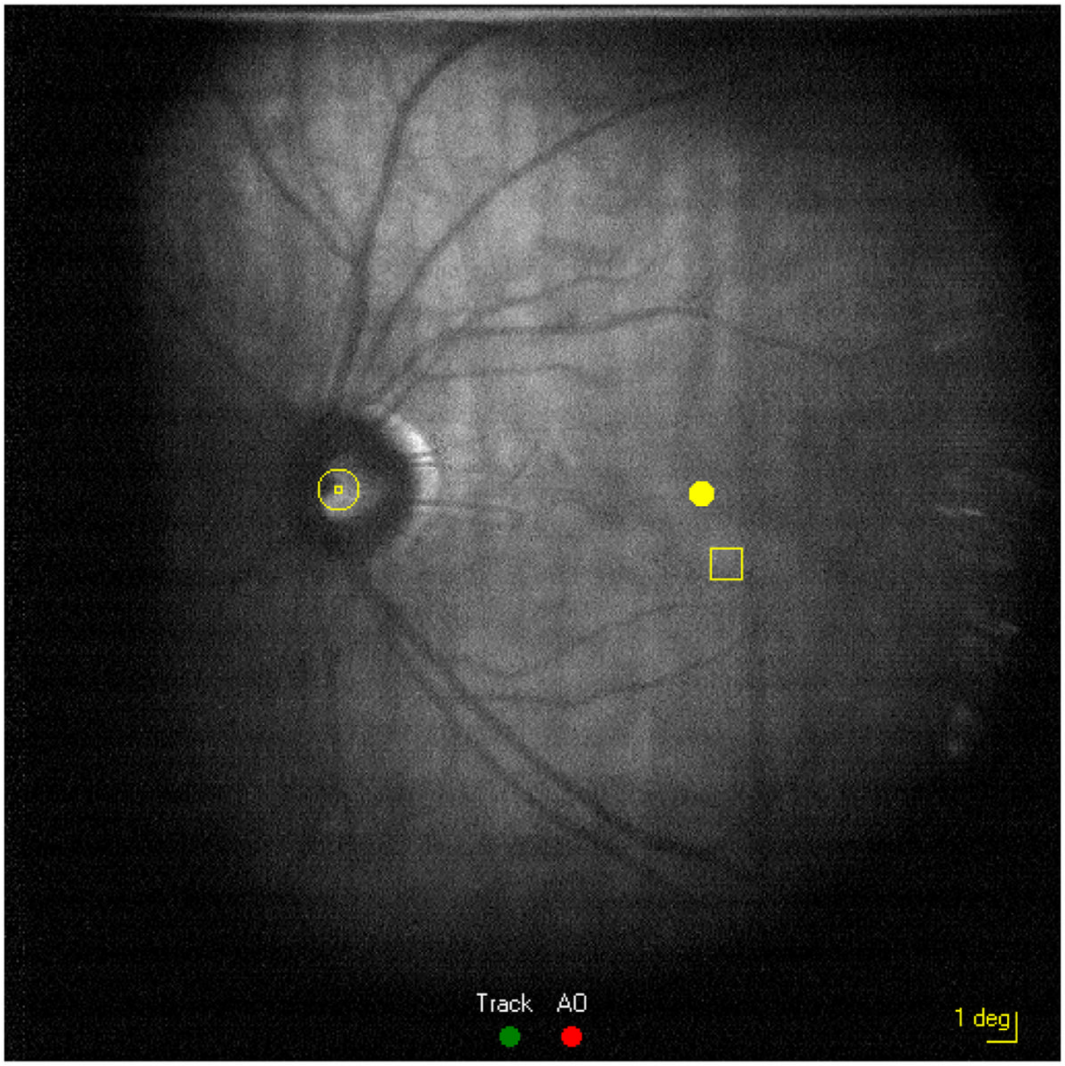

**Fig. 10.**
(2.0 Mb) Video taken from wide-field LSLO during automatic macular montage acquisition. LSLO overlay shows position of tracking beam (○), position of fixation target (●), position of SLO raster (☐ ), scale, and track and AO on (● )/off (●) indicators.

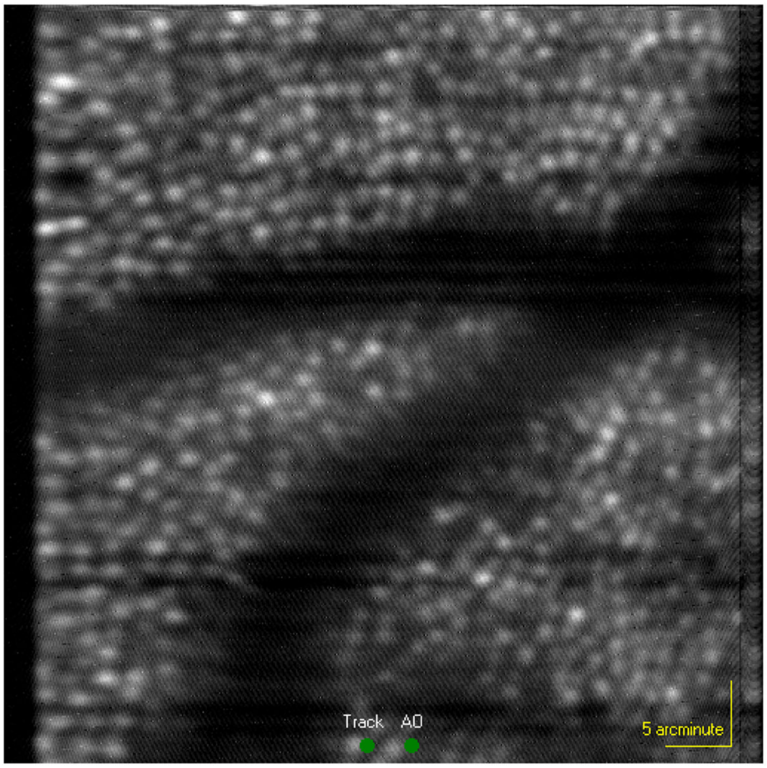

**Fig. 11.**
(3.8 Mb) Video of AOSLO during automatic macular montage acquisition (different subject than Fig. 10).

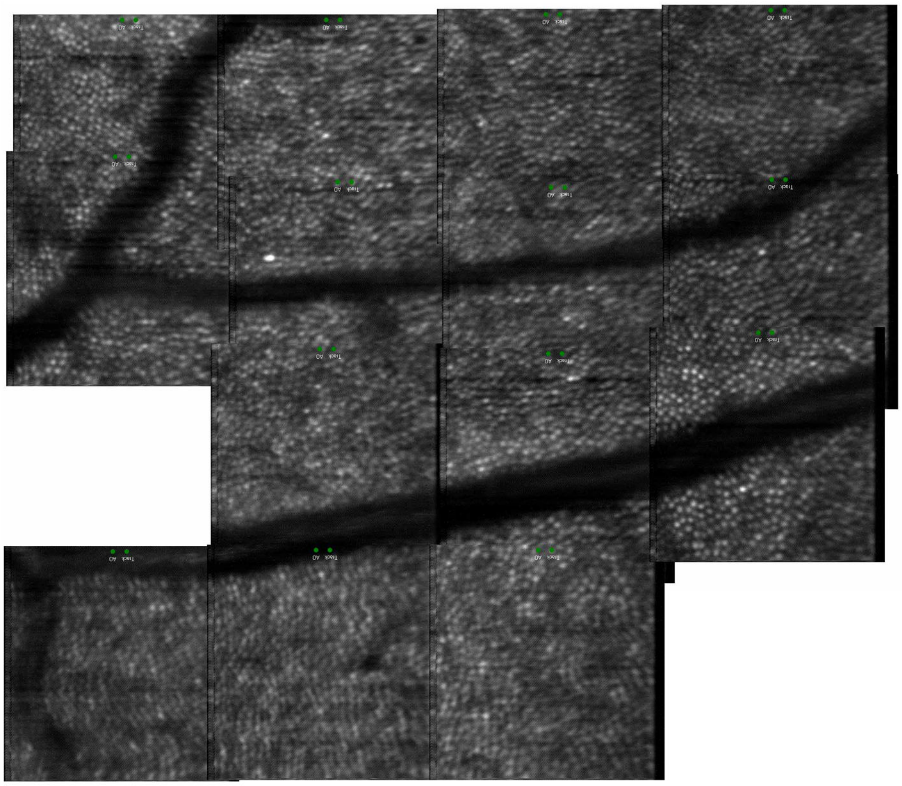

**Fig. 12.**
Macular montage created from video shown in Fig. 11.